

## Article

# Modeling and Experimental Investigations of Nanostructured Ag Thin Films Produced by Oblique-Angle Deposition and Its SERS Performance

Datai Hui <sup>1,†</sup>, Shun Zhou <sup>1,†</sup>, Changlong Cai <sup>1,\*</sup>, Shigeng Song <sup>2,\*</sup>, Zhentao Wu <sup>2</sup>, Jian Song <sup>2</sup>, Da Zhang <sup>1</sup>, Xiao Meng <sup>1</sup>, Bo Lu <sup>2</sup>, Yingbu Duan <sup>1</sup>, Hayrigul Tursun <sup>3</sup> and Des Gibson <sup>2</sup>

<sup>1</sup> School of Opto-electronical Engineering, Xi'an Technological University, Xi'an 710021, China; huidatai\_edu@163.com (D.H.); zhoushun@xatu.edu.cn (S.Z.); ds6652110@163.com (D.Z.); xiaomengxatu@126.com (X.M.); duanyingbu@st.xatu.edu.cn (Y.D.)

<sup>2</sup> Institute of Thin Film, Sensors and Imaging, School of Computing, Engineering and Physical Sciences, University of the West of Scotland, Paisley G72 0LH, UK; Zhentao.Wu@uws.ac.uk (Z.W.); jian.song@uws.ac.uk (J.S.); b00375928@studentmail.uws.ac.uk (B.L.); des.gibson@uws.ac.uk (D.G.)

<sup>3</sup> School of Physics and Information Technology, Shaanxi Normal University, Xi'an 710062, China; hairegul@snnu.edu.cn

\* Correspondence: caichanglong@xatu.edu.cn (C.C.); Shigeng.Song@uws.ac.uk (S.S.); Tel.: +86-02986173178 (C.C.); +44-01418483630 (S.S.)

† D.H. and S.Z. contributed equally to this work and are as co-first authors.



**Citation:** Hui, D.; Zhou, S.; Cai, C.; Song, S.; Wu, Z.; Song, J.; Zhang, D.; Meng, X.; Lu, B.; Duan, Y.; et al. Modeling and Experimental Investigations of Nanostructured Ag Thin Films Produced by Oblique-Angle Deposition and Its SERS Performance. *Coatings* **2021**, *11*, 458. <https://doi.org/10.3390/coatings11040458>

Academic Editor: Alberto Palmero

Received: 2 February 2021

Accepted: 13 April 2021

Published: 15 April 2021

**Publisher's Note:** MDPI stays neutral with regard to jurisdictional claims in published maps and institutional affiliations.



**Copyright:** © 2021 by the authors. Licensee MDPI, Basel, Switzerland. This article is an open access article distributed under the terms and conditions of the Creative Commons Attribution (CC BY) license (<https://creativecommons.org/licenses/by/4.0/>).

**Abstract:** The growth mechanism of nanocolumnar silver thin film deposited on a smooth silicon substrate using electron beam evaporation process at an oblique angle was simulated with the Kinetic Monte Carlo method. Following the simulated silver nanostructured thin film, a further computational simulation was done using COMSOL for surface-enhanced Raman scattering effects. The simulation results were compared against corresponding experimental results, which demonstrated high agreement between simulation results and experimental data. It was found that as the incident deposition angle increased, the density of the Ag thin film significantly decreased and the surface roughness increased. When the incident deposition angle was at 75° and 85°, the resulting nanocolumnar structure was significantly tilted. For Ag thin films deposited at all investigated angles, surface-enhanced Raman scattering effects were observed. Particularly, the Ag nanocolumns deposited at 85° showed remarkable Surface-enhanced Raman Scattering effects. This was seen in both COMSOL simulations and experimental results: Enhancement factors were  $2 \times 10^7$  in COMSOL simulation and  $3.3 \times 10^5$  in the experiment.

**Keywords:** Kinetic Monte Carlo simulation; Oblique-Angle Deposition; silver thin film; nanocolumnar structure; SERS

## 1. Introduction

The Oblique-Angle Deposition (OAD) method is a thin-film deposition method that can be used to obtain a thin-film nanostructure or a specific thin-film surface morphology [1]. Nanostructured films produced by OAD are also known as sculptured thin films [2]. Compared with the traditional deposition method, the vapor-phase atomic beam or ion beam current is incident at an angle to the substrate rather than just being perpendicular to the substrate. The nanostructure, morphology, and porosity of the thin film are formed by the ballistic shadowing effect, which is dependent on the incident angle. Increased incident angle increases the shadowing length, which, in turn, increases the percentage of substrate that is self-blocked from deposition [3]. Therefore, the void area between the columns is increased and the density of the film is reduced [4]. Using this OAD method, a porous nanostructure, different from the traditional dense film, can be obtained. The porous, nanostructured film is not only sculptural but also has anisotropy, controllable

refractive index, and other useful characteristics, which can be widely used for Surface-Enhanced Raman Scattering (SERS), phase retarders, biosensors, optoelectronic crystal devices, virus/bacteria/toxin detections [5–7], optical fiber probes [8], and ultrathin-layer chromatography plates [9]. Among these applications, the SERS [10] sensor is one of the more typical applications of these nanostructured films deposited using OAD method.

Raman spectroscopy is versatile non-destructive testing and molecular recognition technology, which can provide fingerprint information of chemical and biological molecular structures [11]. Ordinary Raman scattering signals are exceedingly weak. However, it was found that the Raman scattering signals can be dramatically enhanced by placing the analyte close to nanostructured metal surfaces, thereby improving detection of trace molecular signatures. Generally, this enhancement of Raman scattering is through the hot spot effect (the strong electromagnetic field area generated by the metal nanostructure). Therefore, exploring and designing an effective metal substrate with a suitable electromagnetic field area is the primary goal of SERS researchers.

Currently, the research on the SERS substrates is mainly through batch experiments. In actual practice, not only are the process parameters during fabrication very complicated and the morphology of SERS substrates difficult to finely control, but the batch experiment itself is a long and tedious process.

In this work, simulation of the growth process of Ag nanostructured films at various incident depositions' angles was done using Kinetic Monte Carlo (KMC) code for the simulation of deposition, diffusion, nucleation, and growth of a film on a substrate, NanoSacle Modeling (NASCAM) [12]. Based on the results of NASCAM simulations, the nanostructured, thin-film physical models were obtained and further simulated for SERS effects using finite element analysis by COMSOL 5.4. Simulation results were then compared to and verified by a corresponding experiment.

## 2. Background of Simulation

### 2.1. Nanostructure Simulation Using the KMC Method

The systematic investigation on the time evolution of nanostructured Ag films deposited using the OAD method at various oblique angles on smooth Si substrate was simulated at the atomic scale using NASCAM software (NASCAM (4.6.2)), which is based on the KMC method [13–15].

Figure 1 displays the geometry schematic of the OAD method in NASCAM. The substrate and circular thermal evaporation source were located at (50, 50, 100) and (50, 50, 0), respectively. The unit of geometry is millimeter. The shape of the vapor distribution emitting from the thermal source was defined by the Cosine law,  $p(\theta) = \cos^n \theta$ , wherein, the directionality of the vapor flow is dependent on the value of  $n$ . The larger the  $n$ , the better the directionality of flow [16]. Besides, the value of  $n$  is related to the shape of the crucible. The deep and narrow crucible has a large  $n$  value, so the evaporation material can be limited to a small divergence angle [16]. In general, the range of the  $n$  is from 1 to 7. In this simulation, to ensure good directional vapor flux and make an agreement with the experimental condition, the value of  $n$  was defined as 7.

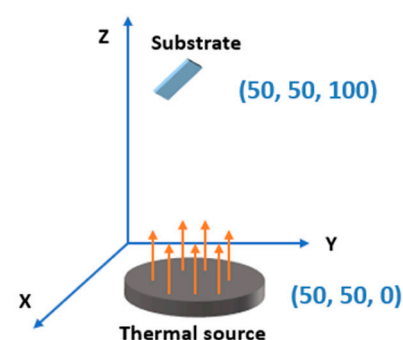


Figure 1. The geometry schematic of the OAD method in NASCAM.

In the KMC method, kinetic events, such as diffusion, can be associated with the physical mechanisms and events that happen in any given direction. The Arrhenius law can be used to describe an elementary event rate for a given event  $i$  [17]:

$$w_i = w_0 \exp(-E_i/k_B T). \quad (1)$$

The  $w_0$  refers to the attempt frequency and  $E_i$  refers to the activation energy for event  $i$ . A type of kinetic event is chosen according to its occurrence probability,  $p_i$ . This is the ratio of the rate of event  $i$  to the total rate (the sum over all event rates) [17]:

$$p_i = N_i w_i / \sum_i N_i w_i \quad (2)$$

where  $N_i$  is the number of atoms and  $w_i$  is the rate of corresponding kinetic event. Table 1 shows the kinetic events with the corresponding activation energies used to simulate the Ag film growth. The activation energy of Ag free diffusion ( $E_{a\_diff}$ ) was estimated to be 0.5 eV by referring to the results of published work [17–19]. In this work, the activation energies were estimated by using the nudged elastic band (NEB) method. Furthermore, a series of activation energies were estimated by referring to the reported values of activation energies in published literature and a general activation energy relationship ( $E_{a\_up}, E_{a\_down} > E_{a\_nn\_inc}, E_{a\_nn\_dec}, E_{a\_detach} > E_{a\_diff}$ , and  $E_{a\_detach} > E_{a\_nn\_dec}$ ; the definitions of each parameters are shown in Table 1) in NASCAM manual [12,18–21]. The substrate temperature was set as 323 K, which made a good agreement with the experiment. In this situation, the probability of an evaporation event occurring was lower than a diffusion event. Therefore, Ag evaporation's activation energy from the substrate or layers ( $E_{a\_evap}$ ) was fixed at 4.5 eV, which was much higher than free diffusion energy ( $E_{a\_diff}$ ). Si substrate bind energy was a default constant value in NASCAM.

**Table 1.** The basic parameters of the Si substrate and substrate physical constant.

Parameters and Physical Constant	Value
Free diffusion ( $E_{a\_diff}$ )	0.5 eV
Hops with an increase or decrease of neighboring atoms number ( $E_{a\_nn\_inc}/E_{a\_nn\_dec}$ )	1.9 eV
Hop down or up from one level to another ( $E_{a\_up}/E_{a\_down}$ )	2.0 eV
Detachment from an island or substrate feature ( $E_{a\_detach}$ )	1.95 eV
Evaporation from the substrate or layers ( $E_{a\_evap}$ )	4.5 eV
Substrate temperature	323 K
Substrate bind energy	3.52 eV

Table 2 displays the deposition parameters in this simulation. The deposition rate was fixed as 0.3 monolayers per second (0.15 nm/s), which was close to the experimental value. The incident energy of the atom was set as 0.6 eV, in accordance with the condition of the e-beam evaporation [16]. The deposition angle was defined as the angle between the incident vapor flux and the substrate normal. Ag thin-film binding energy was predefined in NASCAM as a default value.

**Table 2.** Deposition parameters in simulation.

Deposition Parameters	Value
Thin-film binding energy	2.97 eV
Incident energy of an atom	0.6 eV
Deposition angle	0°/45°/75°/85°
Deposition rate	0.3 mL/s

### 2.2. SERS Performance Simulation Model

Figure 2 displays the geometry schematic of the SERS simulation model. Gaussian beam was incident on the nanostructure. The polarization direction of the incident was defined as the connection direction of nanocolumns. The reason is when the polarization direction of the incident is parallel to the connection direction of the nanocolumns, the nanocolumns will act as dipoles with each other and the plasmon effect will occur on the surface of the nanocolumns, inducing a significant enhancement of the horizontal electromagnetic field. Chosen Gaussian beam and the two-dimensional Gaussian beam expression [22] are shown below:

$$E_{Gauss}(x,y) = E_0 \sqrt{\frac{w_0}{w(y)}} \exp(-x^2/w(y)^2) \exp(-ikx^2/(2R(y)) + i\eta(y)) \quad (3)$$

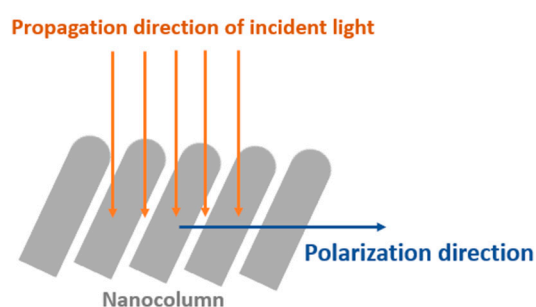


Figure 2. The diagram of nanocolumn array and incident Gaussian beam in COMSOL model.

In this expression,  $w_0$  is the minimum waist,  $w$  is the angular frequency,  $k$  is the wavenumber, and  $\eta(y)$  is the phase correction. The wavefront of the beam is not exactly planar. It propagates like a spherical wave with radius  $R(y)$ .

Plane-wave expansion of Gaussian beam is:

$$E_{PW} = \sum_{j=-M}^M \sum_{k=0}^1 a_{jk} \hat{u}_k(\mathbf{k}_j) \exp(-i(\mathbf{k}_j \cdot \mathbf{r})) \quad (4)$$

where each wave vector  $\mathbf{k}_j$  points in different directions for each value of the index  $j$  and  $a_{jk}$  is the amplitude that has a different value for each wave vector and also for each of the two possible polarization directions per wave vector,  $\hat{u}_k(\mathbf{k}_j)$ .

The wavelength of incident light was chosen as 638 nm since 638 nm is commonly used as excitation wavelength in the Raman spectrum. The propagation medium of electromagnetic waves was defined as air, and the material of nanostructure was defined as Ag. The dispersion formula [23] of the relative dielectric constant of Ag is:

$$\epsilon(\omega) = 1 - \frac{\omega_p^2}{\omega^2} \quad (5)$$

The angular frequency is defined as:

$$\omega = \frac{2\pi c}{\lambda} \quad (6)$$

where  $\omega_p$  is the plasma frequency of the material, the plasma frequency of Ag is about  $\sqrt{21}\omega$ , and the relative dielectric constant obtained is a negative value. For many metals, this phenomenon is normal when the incident light frequency is lower than the plasma frequency.

### 3. Experiment

#### 3.1. Deposition

The Ag nanostructured films were deposited by e-beam evaporation at different vapor incident angles,  $\theta = 0^\circ, 45^\circ, 75^\circ$  and  $85^\circ$ . The tilt angle of the sample can be manually controlled by motion feedthrough. Silver with a purity of 99.99% was used as deposition material. Silicon wafers were used as substrates and a standard substrate cleaning process was performed before film deposition, as follows. A mixture of ether and anhydrous ethanol in a ratio of 1:3 was used to clean the substrate, and then the substrate was put into an ultrasonic cleaner for 2 min. We repeated the steps two times, and, finally, dried the surface with nitrogen gas. The thicknesses of samples were controlled by using a quartz crystal monitor. The current of the electron gun and the system bias voltage were set as 120 mA and 7 kv, respectively. The deposition temperature was fixed as 323 K. The configuration of the OAD system is shown in Figure 3.

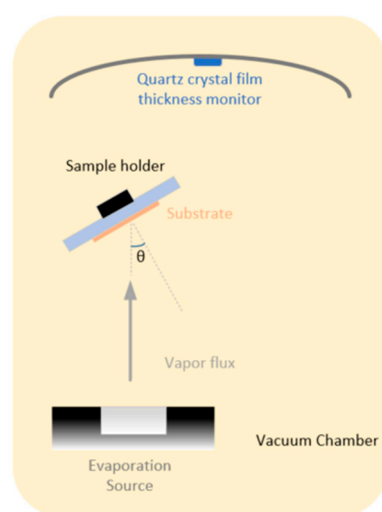


**Figure 3.** The configuration of OAD system.

#### 3.2. Characterization

The SERS was investigated using Rhodamine 6G as a probe molecule at an excitation wavelength of 638 nm. Rhodamine 6G was chosen because it has a relatively large Raman cross section and is commonly used as a Raman probe molecule on silver substrates. A droplet of Rhodamine 6G solution with a concentration of  $10^{-5}$  M was dispensed on the surface of silver samples. Another droplet of Rhodamine 6G solution with a concentration of  $5 \times 10^{-2}$  M was dispensed on a silicon wafer as a reference substrate. For the enhancement factor, the enhancement factor (EF) of the Raman scattering was estimated by the following formula [23].

$$EF = \frac{I_{SERS}/C_{SERS}}{I_{REF}/C_{REF}} \quad (7)$$

where  $I_{SERS}$  and  $C_{SERS}$  are the SERS peak intensity and the concentration of R6G molecules adsorbed on the Ag SERS substrate, respectively.  $I_{REF}$  and  $C_{REF}$  are the normal Raman peak intensity and the concentration adsorbed on the reference substrate, respectively. The Raman system was calibrated by using a silicon standard before silver sample measurements.

The morphology of silver samples was observed by using SEM and the tilt angles of nanocolumns were measured by a free screen protractor software in the SEM pictures and took an average value of several sets of measurements. The surface roughness of the film was measured with a non-contact surface profiler. The fabrication process is shown in Figure 4.

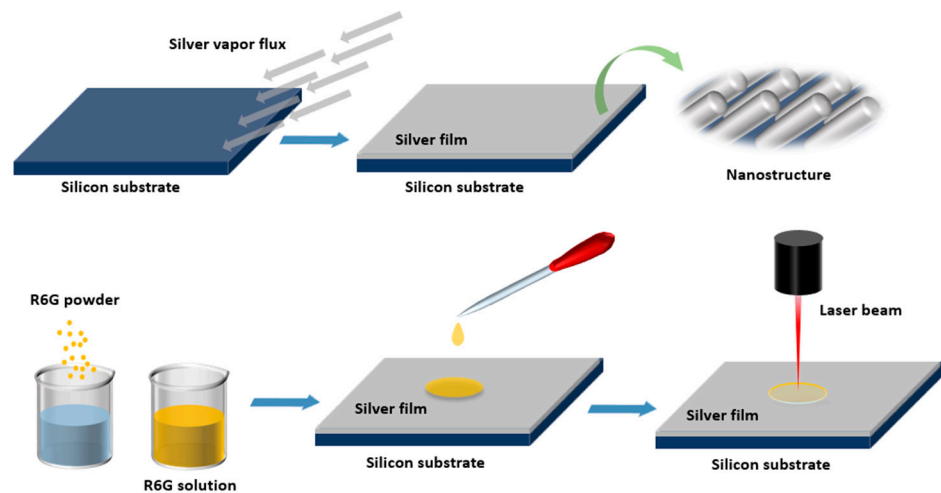


Figure 4. Schematic of fabrication and test process.

## 4. Results and Discussions

### 4.1. Comparison of KMC Simulation and Experimental Result

#### 4.1.1. KMC Simulation Results

Figures 5 and 6 display the film growth results at different stages. Figure 5 demonstrates that, in the initial stage of islands' growth, in which the size of deposited monolayers was 0.5 mL, owing to the diffusion effect between the atoms and the substrate, the atoms can migrate and adsorb each other. However, due to a few numbers of deposited atoms at this stage, it was difficult to form a continuous and prominent island-like structure. Nevertheless, it is worth mentioning that when the deposition angle was  $85^\circ$ , the initial island structures on the substrate were slightly larger than the islands obtained from other deposition angles. This phenomenon was explained to be the initial shadowing effect that prevented free diffusion of some atoms on the substrate. Thus, it was easier for atoms to be captured by large atomic groups.

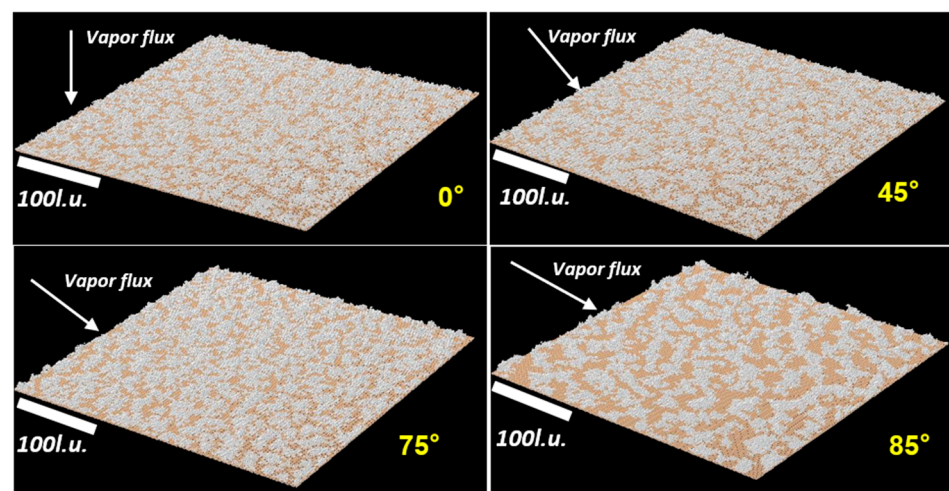
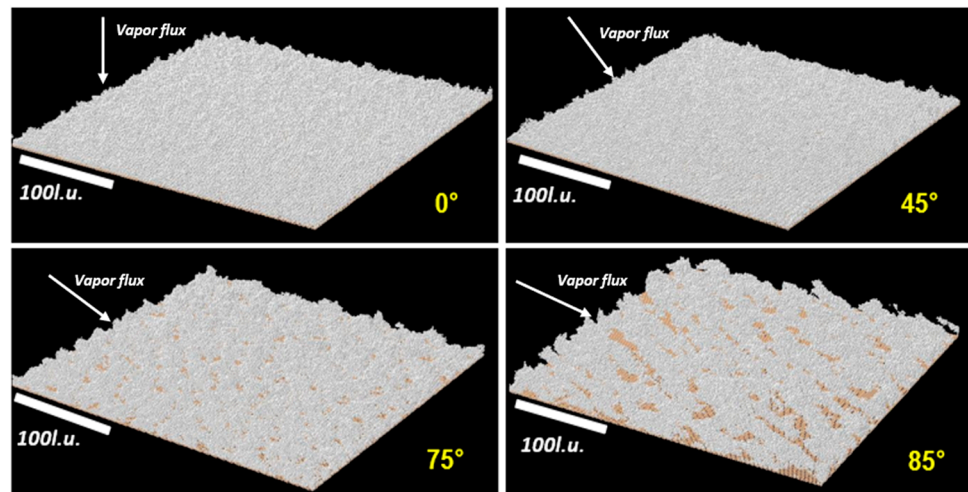
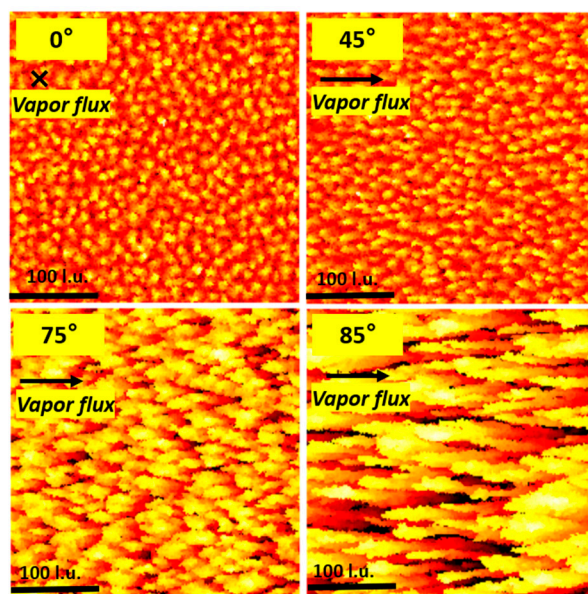


Figure 5. Film growth simulation results at the initial island growth stage (0.5 mL) under different deposition angles.



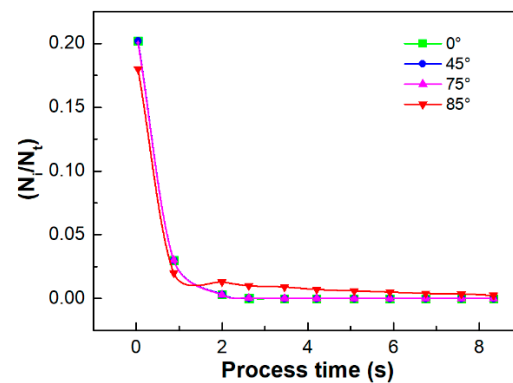
**Figure 6.** Film growth simulation results at the initial nanostructure growth stage (2.5 mL) under different deposition angles.

Figure 6 displays the film growth results under various deposition angles at the initial nanostructures' growth stage, in which the size of deposited monolayers was 2.5 mL. In this stage, more atoms covered the substrate, forming a layered film or initial nanostructure. Figure 6 indicates that when depositing at a low angle, the deposited atoms can diffuse and combine readily with each other on the substrate due to the relatively weak shadowing effect, resulting in a continuous layered film without any nanostructure. However, the film obtained at a high deposition angle showed prominent initial nanocolumn structures. The reason is the shadowing effect is drastically enhanced by increased deposition angle, inducing many atoms' failing to diffuse and migrate into the shadowing area. As the deposition process continued, the atoms continuously adsorbed and deposited on the atomic group, resulting in oriented growing along a specific direction and forming the initial nanostructures. Figure 7 gives the top view of the initial nanostructure of Ag thin film. It can be observed clearly that the initial nanostructure of Ag thin film became more significant due to a more substantial shadowing effect, which was related to increased deposition angles.



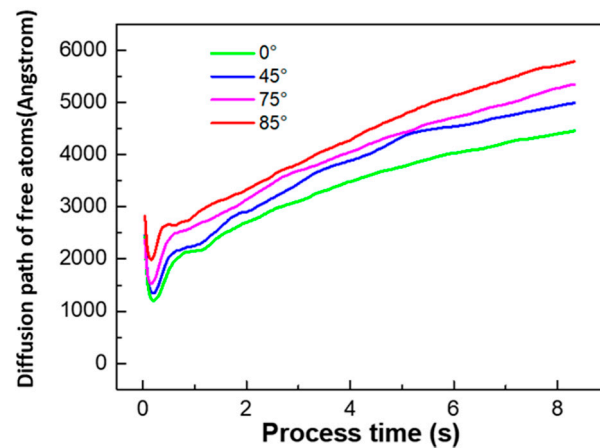
**Figure 7.** The top views of the initial nanostructure of the silver film under different deposition angles in simulation.

Figure 8 displays the ratio of the number of islands ( $N_i$ ) to the total number of atoms deposited at the same moment ( $N_t$ ) on the substrate at the initial growth stage. It is worth noting that the software defines an island as two or more particles being within each nearest lattice points. (The island size, as defined, started at 2 atoms) [12,17]. The island number as used in Figure 8 was an averaged value from several simulations that were conducted. Figure 8 demonstrates that the ratio of number of islands to number of atoms decreased with the deposition time during the initial growth stage. In this stage, atoms combined, nucleating to form the initial island-like structure. As the number of deposited atoms increases, these independent island-like structures can aggregate into atomic layers or can form a continuous film, resulting in a decrease in the ratio of number of islands to number of atoms. It can also be observed that the ratio eventually decreased to 0 (i.e., no more islands, just a continuous film) at the deposition angles of  $0^\circ$ ,  $45^\circ$ , and  $75^\circ$ , whereas when the deposition angle was  $85^\circ$ , no continuous film was formed under our simulation conditions. For simulations done at deposition angle of  $85^\circ$ , the ratio dropped sharply but did not reach 0. This result indicates that under high-angle deposition, the gap/shadowed areas between the tilted nanocolumns were relatively large and it was difficult for new incident atoms to reach these shadowed gaps, therefore, inhibiting formation of continuous film.



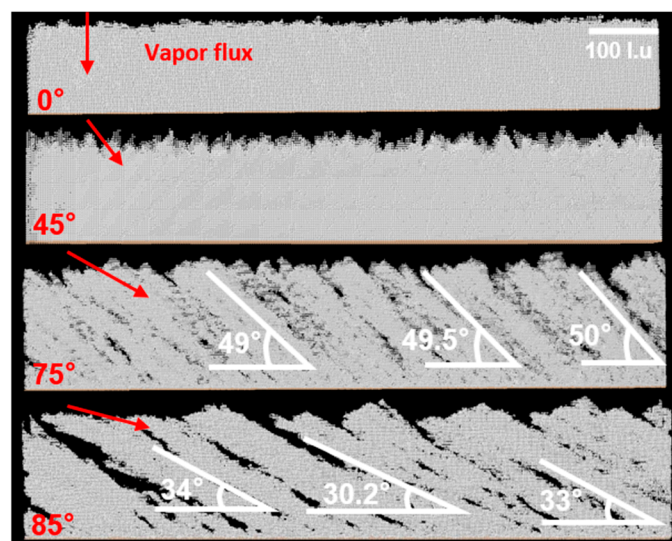
**Figure 8.** The curves of the ratio of the number of islands ( $N_i$ ) to the total number of atoms deposited at the same moment ( $N_t$ ) under various deposition angles at the initial growth stage.

Figure 9 shows the relationship between the free atoms' mean diffusion path on the substrate and the deposition time. The calculation method of mean diffusion path in NASCAM was demonstrated as follows. For each atom, the number of jumps between the deposition and the first attachment and between a possible next detachment and further attachments was calculated. Then, this number was divided by the number of periods of time when the atom was free [12,17]. Obviously, the atom was free before the first attachment and between further detachments and subsequent attachments. In this way, a mean diffusion path for a given atom can be estimated. The mean path was then obtained via statistical approach for all atoms in the system that was simulated. The value of mean diffusion path presented in Results was an averaged value from several simulations conducted. It can be found from Figure 9 that a longer diffusion distance of free atoms on the substrate was produced by the increase of the deposition angle. The reason is that, under large-angle deposition, the shadowing effect is extremely strong and the shadowing area is relatively large, which can provide sufficient area for free atoms to diffuse a longer distance on the substrate before combining with other atoms.



**Figure 9.** The curves of the free atoms' mean diffusion path at the initial stage of film growth under different deposition angle.

Figure 10 shows the final results of the nanostructured film in simulation. It suggests that the film had a more significant nanocolumnar structure with the increase of the deposition angle. To be specific, a flat and smooth film surface was obtained at the deposition angle of  $0^\circ$ . When the deposition angle was increased to  $45^\circ$ , many nano-tips appeared on the surface of the film, although there was still no significant nanocolumnar structure. However, the film had a significant tilted nanocolumnar structure when depositing at the angles of  $75^\circ$  and  $85^\circ$ . The tilt angle of nanocolumn was defined as the angle between the nanocolumn and substrate, and the angles were measured by a free protractor software and took the average of several sets of measurements. It was found that the average tilt angles of nanocolumn at the angles of  $75^\circ$  and  $85^\circ$  were  $49.1^\circ$  and  $32.8^\circ$ , respectively. Figures 11 and 12 show the film's surface roughness and density as a deposition time function. The results show that the thin-film surface roughness and thin-film density were associated with the deposition angle. Thin-film surface roughness dramatically increased with deposition angle, especially when the deposition angle was greater than  $45^\circ$ . Besides, an increase in deposition angle led to a decrease in film density. These results are related to the shadowing effect. The length of the shadowing area increased with the deposition angle. Therefore, atoms could enter the shadowing area only through the diffusion effect under high-angle deposition, which reduced the number of atoms in the shadowing area and resulted in a decrease in film density.



**Figure 10.** Simulated nanostructure thin film under different deposition angles.

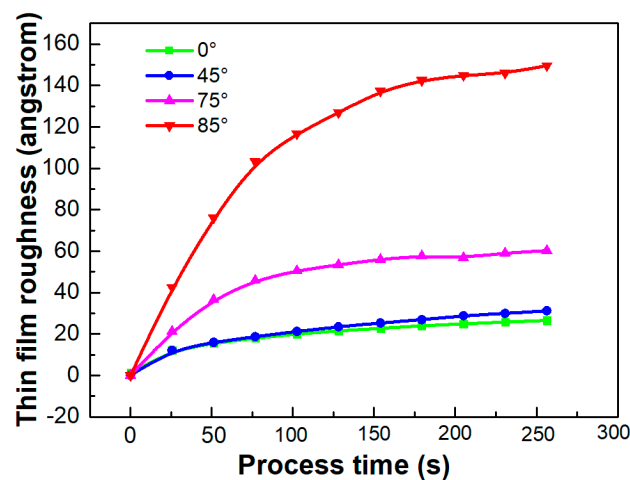


Figure 11. The relationship between surface roughness of silver film and process time.

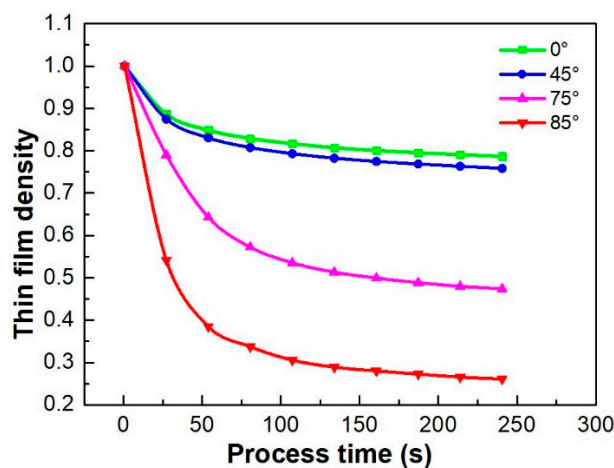


Figure 12. The relationship between thin-film density and process time.

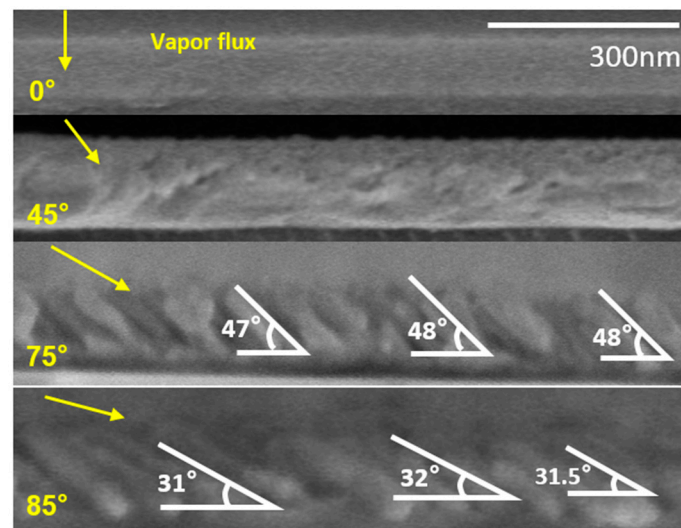
#### 4.1.2. Experimental Results

Figure 13 shows experimental results of nanostructured Ag film obtained under different deposition angles. The films only obtained at 75° and 85° had the obvious tilted nanocolumnar structure. The tilt angle of nanocolumn was defined as the angle between the nanocolumn and substrate, and it was found that the average tilt angles of the nanocolumns obtained under 75° and 85° from simulation and experiment showed a good consistency, wherein the tilt angles in simulation were 49.1° and 32.8° and the tilt angles in experiment were 47.4° and 31.8°, respectively. These results also indicated that there was a relatively good agreement with the tilt angle predicted by the law of cosine (Equation (8)) [24].

$$\beta = \alpha - \sin^{-1}\left(\frac{1 - \cos\alpha}{2}\right) \quad (8)$$

where  $\alpha$  is the deposition angle and  $\beta$  is the angle between the nanocolumn and substrate normal. So, the tilt angle of nanocolumn was  $(\pi/2) - \beta$ . Table 3 displays the comparison of tilt angle of nanocolumn between simulation, experiment, and theoretical estimation (Equation (8)). It indicates that the tilt angles of nanocolumn obtained at 85° in simulation and experiment demonstrated a high consistency with theoretical estimation. However, when the deposition angle was 75°, there was a difference between the theoretical estimation and simulated and experimental results. The reason is that the cosine law focuses on and considers the shadowing effect's influence on the tilt angle. Especially when a very high deposition angle can lead to an extremely strong shadowing effect, the column tilt

angle predicted by this equation is very accurate [1]. However, 75° is not a very high angle, which cannot lead to an extremely strong shadowing effect. So, the tilt angles predicted by the cosine law did not totally agree with experimental and simulation results. This difference of tilt angle of nanocolumn was also reported in other published papers and references [1,25]. Besides, the predicted angle by Equation (8) is a reference data for this work, and the simulation results and experiment results achieved a good agreement in this work. The KMC simulation results shown in Figure 10 and the experimental results shown in Figure 13 demonstrate that the obvious nanocolumn structure only was observed at high angle of deposition by the OAD method, which was similar to the relevant published literature in this research area. In particular, the nanostructures had the same growth pattern and trend due to the shadowing effect under high angle deposition. Although the tilted angles of nanocolumn had a little difference, since the difference of film material and deposition method such as the tilt angle was 34° in Dr. Song's work and 38° in Dervaux's work at 85° deposition angle, it still implies that the results in this work agreed with reported work [1,2,21,26].



**Figure 13.** Ag thin film obtained from experiment under various deposition angles.

**Table 3.** Comparison of nanocolumns' average tilt angle between simulation, experiment, and theoretical estimation.

Deposition Angle	Simulation(Average)	Experiment(Average)	Theoretical Estimation
75°	49.1°	47.4°	40°
85°	32.8°	31.8°	33°

Table 4 shows a comparison of the surface roughness of simulation and the experimental results. Both of the roughness values calculated from NASCAM simulations and experiment were defined as the arithmetic average of the absolute value of the surface height deviation,  $RMS = \sqrt{\langle h^2 \rangle - \langle h \rangle^2}$ , where  $h$  is the local thickness of the film and  $\langle \rangle$  means the averaging over the whole film. The roughness unit in simulation was lattice unit (l.u.), which is defined as the smallest repeating unit having the full symmetry of the structure [12]. Typical RMS roughness values ranging from 2–3 to 20 nm have been reported for OAD thin films prepared by e-beam evaporation [27,28]. This table demonstrates that the trend of surface roughness in the simulation results was in approximate agreement with experiment results: The thin-film surface roughness increased with the increasing of the incident deposition angle.

**Table 4.** Comparison of surface roughness of simulation results and the experimental results.

Deposition Angle	Thin-Film Surface Roughness (Simulation)	Estimation from Simulation (nm)	Thin-Film Surface Roughness (Experiment)
0°	6.5 l.u	2.6 nm	1.8 nm
45°	7.6 l.u	3.1 nm	2.1 nm
75°	14.7 l.u	6.0 nm	6.7 nm
85°	36.6 l.u	14.9 nm	18 nm

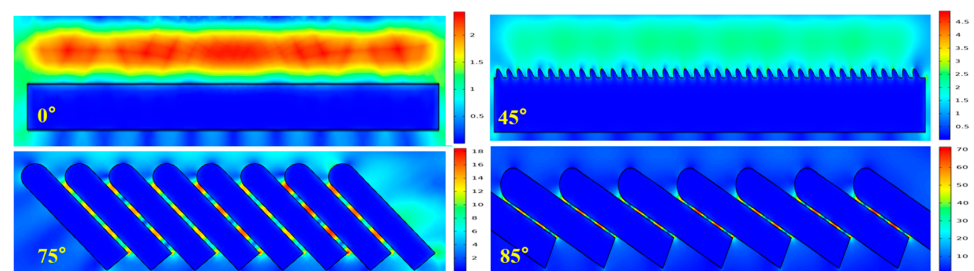
Note: The roughness in lattice unit can be estimated to nanometer unit by multiplying the lattice constant of Ag. For example, the film roughness obtained at 85° was 36.6 l.u. By multiplying the lattice constant of Ag (0.408 nm), the film roughness was estimated to 14.9 nm.

#### 4.2. Comparison of SERS Performance Simulation Results and Experimental Results

According to the KMC simulation results, approximated nanostructure models were carried out and then the local enhanced electric field of nanostructures was simulated after being irradiated by the Gaussian beam. The contribution of the electromagnetic field in Raman scattering can be expressed as:

$$EF_{EM} = |E(\omega)|^2 |E(\omega')|^2 \quad (9)$$

where  $E(\omega)$  is the electric field intensity of incident light and  $E(\omega')$  is the electric field intensity of scattered light with frequency  $\omega'$ . Since the frequency of the scattered light and the frequency of the incident light were relatively close, it can be considered that the contribution of the electromagnetic field in the Raman spectrum was proportional to the fourth power of the intensity of the incident electric field. Figure 14 displays the approximated nanostructure models based on KMC results and the simulation results of the electric field distribution of the enhanced local electric field. As shown in Figure 14, the enhanced electric field distribution demonstrated that the strong enhanced electric field only occurred between the nanocolumn obtained under high-angle deposition. The reason is that the dipole coupling electromagnetic excitation occurred between the nanocolumns and plasmon resonance occurred on the surface of nanocolumns.

**Figure 14.** Electric field distribution diagram of Ag film obtained from different deposition angles.

The curves in Figure 15 show the local enhanced electric field intensity of nanostructure film obtained under different deposition angles in simulation. From the figure, when the deposition angles were 0° and 45°, the intensity of the local enhanced electric field was about 3 to 5 times compared to the incident electric field. However, when the deposition angles were 75° and 85°, the intensity was 18 times and 69 times compared to the incident electric field. According to the contribution of the electromagnetic field in Raman scattering that is proportional to the fourth power of the incident electric field intensity, the enhancement factor of Raman scattering was about  $10^2$  when the deposition angles were 0° and 45°. However, the enhancement factor of Raman scattering had a significant promotion, such that the enhancement factor could reach  $10^5$  and  $2 \times 10^7$  when the deposition angles were 75° and 85°, respectively.

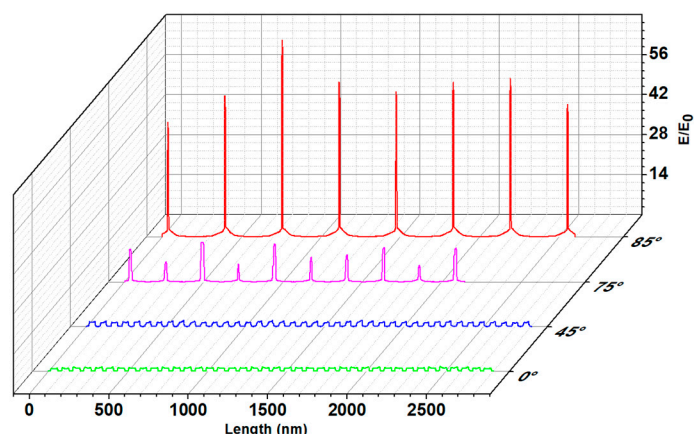


**Figure 15.** Curves of the local electric field along the array direction generated by the nanocolumns obtained under different deposition angles in simulation.

Figure 16 demonstrates the SERS performance in the experiment. From the experimental results, it can be found that the Ag film deposited at  $85^\circ$  angle has a remarkable SERS intensity and the simulation results agreed with the experimental results. Enhancement factor of the Raman scattering was also estimated by the formula 5. Herein, the reference concentration of R6G was determined to be  $10^{-5}$  M for  $C_{SERS}$  and  $5 \times 10^{-2}$  M for  $C_{REF}$ . For maximum Raman intensity peak, the maximum enhancement factor was estimated to  $3.3 \times 10^5$ .

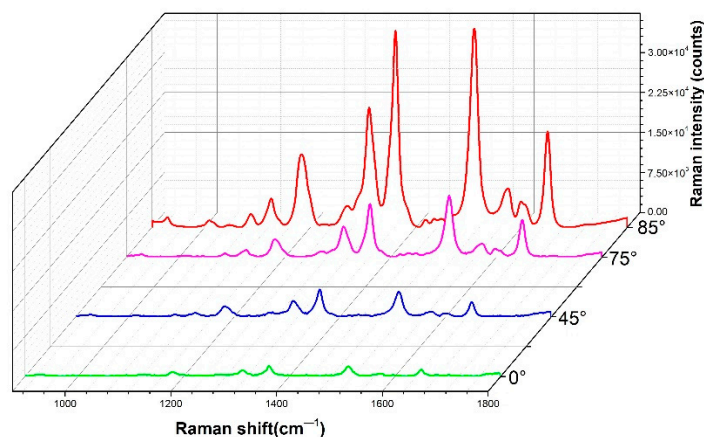


**Figure 16.** SERS performance obtained from the experiment.

From the comparison of simulation and experimental results for Ag nanocolumnar thin films deposited at all investigated angles, it was found that Ag thin-film nanocolumns were deposited at an angle of  $85^\circ$ , had the strongest local electric field enhancement and SERS intensity, followed by deposition at  $75^\circ$ , and there was no significant promotion of SERS intensity at  $45^\circ$  and  $0^\circ$  deposition. The SERS enhancement factor had a drastic promotion with the increase of deposition angle. This result is also similar to other reported work that nanostructured or sculptured film obtained under high-angle deposition has a better SERS performance [2,3]. The reason for the promotion of film SERS performance is the low density and separation of nanocolumns of the film under high-angle deposition. After the film was irradiated by incident light, dipole coupling electromagnetic excitation occurred between the separation nanocolumns and plasmon resonance occurred on the surface of nanocolumns. The electrons on the film surface collectively moved to form surface plasma, which coupled and oscillated with the incident and scattered photoelectric fields to generate a strong local electric field to enhance the SERS intensity.

## 5. Conclusions

The growth mechanism of nanocolumnar Ag thin film deposited on a smooth Si substrate using electron beam evaporation process at an oblique angle was simulated with the KMC method. Following the simulated silver nanostructured thin film, a further computational simulation was done using COMSOL for SERS performance. The experimental results were compared with corresponding simulation results and showed a good agreement. The conclusions were drawn as follows.

Firstly, an increase of deposition angle induces an increase of the Ag thin-film surface roughness, and a high deposition angle leads to a significant decrease of thin-film density. The initial nanostructure formation at the early stage of film growth is caused by the strong ballistic shadowing effect associated with oblique-angle deposition.

Secondly, the KMC simulation results showed good consistency with experimental results, either the morphologies or tilt angle of nanocolumns. It is worth noting that when the deposition angles were  $75^\circ$  and  $85^\circ$ , the Ag film had an obvious nanocolumnar structure and the tilt angles of the nanocolumns obtained both from simulation and experiment were followed by the cosine law.

Furthermore, after being irradiated by a Gaussian beam with a wavelength of 638 nm, the Ag film obtained at a high deposition angle had a relatively strong, locally enhanced electric field intensity than a low deposition angle one. For Ag nanocolumnar thin films deposited at all investigated angles, nanostructured Ag film only obtained at  $85^\circ$  deposition angle gave the strongest SERS performance, both in simulation and experiment.

Finally, the NASCAM simulation greatly supported the experimental observation, especially for film growth process and nanostructures. This implies that the KMC simulations realistically reproduce the island formation, atomics' diffusion process, ballistic understanding of the mechanisms governing the growth of nanostructured Ag film. Meanwhile, SERS performance of nanostructured film based on KMC simulations showed good consistency with experimental data, which provides a convincing example for us. This KMC/COMSOL modeling and experimental method can be used in the future to investigate nanostructured film applications.

**Author Contributions:** Conceptualization, D.H., S.S. and S.Z.; methodology, D.H., S.Z. and S.S.; software, H.T., D.H., S.Z. and S.S.; validation, D.H., Z.W. and J.S.; formal analysis, D.H. and S.Z.; investigation, D.H., S.S., S.Z. and C.C.; resources, H.T., D.Z., X.M. and Y.D.; data curation, D.H., S.Z., C.C., S.S., Z.W. and X.M.; writing—original draft preparation, D.H.; writing—review and editing, S.S., B.L. and S.Z.; visualization, S.S. and C.C.; supervision, D.H., C.C. and S.S.; project administration, S.S., C.C. and D.G.; funding acquisition, C.C. and S.S. All authors have read and agreed to the published version of the manuscript.

**Funding:** This work was supported by School of Opto-electronical Engineering, Xi'an Technological University; Institute of Thin Film, Sensors and Imaging, School of Computing, Engineering and Physical Sciences, University of the West of Scotland; and General Project of Shaanxi Provincial Department of Science and Technology in the Industrial Field (Project Number: 2020GY-045).

**Institutional Review Board Statement:** Not applicable.

**Informed Consent Statement:** Not applicable.

**Data Availability Statement:** The data presented in this study are available on request from the corresponding author.

**Acknowledgments:** Thanks to Hayrigul Tursun, School of Physics and Information Technology, Shaanxi Normal University, for providing the workstation for COMSOL computing.

**Conflicts of Interest:** The authors declare no conflict of interest.

## References

1. Hawkeye, M.M.; Taschuk, M.T.; Brett, M.J. *Glancing Angle Deposition of Thin Films: Engineering the Nanoscale*; John Wiley & Sons: Hoboken, NJ, USA, 2014.
2. Song, S.; Keating, M.; Chen, Y.; Placido, F. Reflectance and surface enhanced Raman scattering (SERS) of sculptured silver films deposited at various vapor incident angles. *Meas. Sci. Technol.* **2012**, *23*, 084007. [CrossRef]
3. Keating, M.; Song, S.; Wei, G.; Graham, D.; Chen, Y.; Placido, F. Ordered Silver and Copper Nanorod Arrays for Enhanced Raman Scattering Created via Guided Oblique Angle Deposition on Polymer. *J. Phys. Chem.* **2014**, *118*, 4878–4884. [CrossRef]
4. Chaney, S.B.; Shanmukh, S.; Dluhy, R.A.; Zhao, Y.P. Aligned silver nanorod arrays produce high sensitivity surface-enhanced Raman spectroscopy substrates. *Appl. Phys. Lett.* **2005**, *87*, 031908. [CrossRef]
5. Karunasiri, R.P.U.; Bruinsma, R.; Rudnick, J. Thin-film growth and the shadowing instability. *Phys. Rev. Lett.* **1989**, *62*, 788–791. [CrossRef]
6. Driskell, J.D.; Zhu, Y.; Kirkwood, C.D.; Zhao, Y.; Dluhy, R.A.; Tripp, R.A. Rapid and Sensitive Detection of Rotavirus Molecular Signatures Using Surface Enhanced Raman Spectroscopy. *PLoS ONE* **2010**, *5*, e10222. [CrossRef]
7. Hennigan, S.L.; Driskell, J.D.; Dluhy, R.A.; Zhao, Y.; Tripp, R.A.; Waites, K.B.; Krause, D.C. Detection of Mycoplasma pneumoniae in Simulated and True Clinical Throat Swab Specimens by Nanorod Array-Surface-Enhanced Raman Spectroscopy. *PLoS ONE* **2010**, *5*, e13633. [CrossRef]
8. Wu, X.; Gao, S.; Wang, J.-S.; Wang, H.; Huang, Y.-W.; Zhao, Y. The surface-enhanced Raman spectra of aflatoxins: Spectral analysis, density functional theory calculation, detection and differentiation. *Analyst* **2012**, *137*, 4226–4234. [CrossRef] [PubMed]
9. Zhu, Y.; Dluhy, R.A.; Zhao, Y. Development of silver nanorod array based fiber optic probes for SERS detection. *Sens. Actuators B Chem.* **2011**, *157*, 42–50. [CrossRef]
10. Chen, J.; Abell, J.; Huang, Y.-W.; Zhao, Y. On-Chip Ultra-Thin Layer Chromatography and Surface Enhanced Raman Spectroscopy. *Lab Chip* **2012**, *12*, 3096–3102. [CrossRef]
11. Moskovits, M. Surface-enhanced Raman spectroscopy: A brief retrospective. *J. Raman Spectrosc.* **2005**, *36*, 485–496. [CrossRef]
12. NASCAM. Available online: <http://www.unamur.be/sciences/physique/pmr/telechargement/logiciels/nascam> (accessed on 15 January 2021).
13. Claassens, C.H.; Hoffman, M.J.H.; Terblans, J.J.; Swart, H.C. Kinetic Monte Carlo Simulation of the Growth of Various Nanostructures through Atomic and Cluster Deposition: Application to Gold Nanostructure Growth on Graphite. *J. Phys. Conf. Ser.* **2006**, *29*, 185–189. [CrossRef]
14. Tan, X.; Zhou, Y.; Zheng, X. Dependence of morphology of pulsed-laser deposited coatings on temperature: A kinetic Monte Carlo simulation. *Surf. Coat. Technol.* **2005**, *197*, 288–293. [CrossRef]
15. Trushin, O.; Karim, A.; Kara, A.; Rahman, T.S. Self-learning kinetic Monte Carlo method: Application to Cu (111). *Phys. Rev. B* **2005**, *72*. [CrossRef]
16. Ohring, M. *Materials Science of Thin Films*; Academic Press: Cambridge, MA, USA, 2001.
17. Lucas, S.; Moskovkin, P. Simulation at high temperature of atomic deposition, islands coalescence, ostwald and inverse ostwald ripening with a general simple kinetic monte carlo code. *Thin Solid Film.* **2010**, *518*, 5355–5361. [CrossRef]
18. De Miguel, J.J.; Sanchez, A.; Cebollada, A.; Gallego, J.M.; Ferron, J.; Ferrer, S. The surface morphology of a growing crystal studied by thermal energy atom scattering (TEAS). *Surf. Sci.* **1987**, *189*, 1062–1068. [CrossRef]
19. Antczak, G.; Ehrlich, G. *Surface Diffusion: Metals, Metal Atoms, and Clusters*; Cambridge University Press: Cambridge, UK, 2010; pp. 295–300.
20. Askill, J. *Tracer Diffusion Data for Metals, Alloys, and Simple Oxides*; Springer: New York, NY, USA, 1970.
21. Dervaux, J.; Cormier, P.-A.; Moskovkin, P.; Douheret, O.; Konstantinidis, S.; Lazzaroni, R.; Lucas, S.; Snyders, R. Synthesis of nanostructured Ti thin films by combining glancing angle deposition and magnetron sputtering: A joint experimental and modeling study. *Thin Solid Film.* **2017**, *636*, 644–657. [CrossRef]
22. Parthasarathy, H. *Waves and Optics*; CRC Press: London, UK, 2021.
23. Kneipp, K. Surface-enhanced Raman scattering. *Phys. Today* **2007**, *11*, 40–46. [CrossRef]
24. Tait, R.N.; Smy, T.; Brett, M.J. Modelling and characterization of columnar growth in evaporated films. *Thin Solid Film.* **1993**, *226*, 196–201. [CrossRef]
25. Hin, O.M.C. Metal Nanostructures Made by Oblique Angle Deposition on Templates for Solid State Surface Enhanced Raman Spectroscopy Substrates. Ph.D. Thesis, University of the West of Scotland, Glasgow, UK, 2019.
26. Alvarez, R.; Garcia-Martin, J.M.; Macias-Montero, M.; Gonzalez-Garcia, L.; González, J.C.; Rico, V.J.; Perlich, J.; Cotrino, J.; González-Elipse, A.R.; Palmero, A. Growth regimes of porous gold thin films deposited by magnetron sputtering at oblique incidence: From compact to columnar microstructures. *Nanotechnology* **2013**, *24*, 45604. [CrossRef]
27. Dalla Torre, J.; Gilmer, G.H.; Windt, D.L.; Kalyanaraman, R.; Baumann, F.H.; O’Sullivan, P.L.; Sapjeta, J.; Díaz de la Rubia, T.; Djafari Rouhani, M. Microstructure of thin films sputtered onto inclined substrates: Experiments and atomistic simulations. *J. Appl. Phys.* **2003**, *94*, 263–271. [CrossRef]
28. Rico, V.J.; Borrás, A.; Yubero, F.; Espinos, J.P.; Frutos, F.; González-Elipse, A.R. Wetting Angles on Illuminated Ta<sub>2</sub>O<sub>5</sub> Thin Films with Controlled Nanostructure. *J. Phys. Chem. C* **2009**, *113*, 3775–3784. [CrossRef]